Phys Chem Minerals (2002) 29: 331–340
DOI 10.1007/s00269-002-0241-y

ORIGINAL PAPER

F. Cámara · M. A. Carpenter · M. C. Domeneghetti
V. Tazzoli

Non-convergent ordering and displacive phase transition in pigeonite: in situ HT XRD study

Received: 23 July 2001 / Accepted: 1 November 2001

Abstract A natural Ca-rich pigeonite ($En_{47}Fs_{43}Wo_{10}$), free of augite exsolution products, was studied by in situ high-temperature single-crystal X-ray diffraction. The sample, monoclinic $P2_1/c$ ($a = 9.719(7)$ Å, $b = 8.947(9)$ Å, $c = 5.251(3)$ Å, $\beta = 108.49(5)$, $V = 433.0(6)$ Å^3), was annealed up to 1000 °C to induce a phase transition from $P2_1/c$ to $C2/c$ symmetry. Complete single-crystal X-ray diffraction data collections were carried out in situ at 650, 750, 850 and 950 °C after the crystal had reached equilibrium for the Fe–Mg intracrystalline exchange reaction at each temperature. The variation, with increasing temperature, of lattice parameters, of intensity of *hkl* reflections with $h + k = 2n + 1$ (which vanish at high temperature) and of some geometrical parameters from structure refinement, showed that the displacive phase transition $P2_1/c \leftrightarrow C2/c$ was continuous in character. This contrasts with the first-order character for the HT phase transition in pigeonite containing significantly less calcium.

Keywords Pigeonite · In situ HT-XRD · Phase transition · Order-disorder

Supplementary material Table 6: Observed and calculated structure factors for *hga* BTS-308 n.16 (room *T*). They have been deposited in electronic form and can be obtained from http://link.springer.de/link/service/journals/00269/index.htm

F. Cámara (✉)
CNR-Centro di Studio per la Cristallochimica e la Cristallografia,
Via Ferrata 27100-Pavia, Italy
E-mail: camara@crystal.unipv.it
Tel.: +39 0382 505891
Fax: +39 0382 505887

M. A. Carpenter
Dept. Earth Sciences,
University of Cambridge, Downing St.,
Cambridge CB2 3EQ,UK

M. C. Domeneghetti · V. Tazzoli
Dip. Scienze della Terra, Università di Pavia,
Via Ferrata 27100-Pavia, Italy

Introduction

Many thermodynamic studies have been carried out on clinopyroxenes due to their ubiquitous occurrence in terrestrial and extraterrestrial rocks. These studies have been used to provide evidence for the *P–T–t* paths of pyroxene-bearing rocks and to reconstruct geological processes. A frequent clinopyroxene in volcanic rocks is pigeonite [(Mg, Fe^{2+}, Ca)(Mg, Fe^{2+})(Si_2O_6)]. At high temperature it crystallizes as monoclinic with space group $C2/c$. Silicon enters tetrahedra linked in chains that extend along the *c* axis while Ca, Mg and Fe occupy two symmetrically different sites: M1, 6-coordinated and M2, 6 + 2-coordinated. Ca may be present in concentrations up to ~0.2 apfu and orders in the larger M2 site. Fe and Mg atoms partition between M1 and M2 sites, following a temperature-dependent ordering process. As temperature decreases, Fe tends to order in the large M2 site, while Mg orders in the smaller M1 site. This process can be described using an order parameter Q_{OD} expressed as:

$$Q_{OD} = \frac{X_{Fe}^{M2} - X_{Fe}^{M1}}{X_{Fe}^{M2} + X_{Fe}^{M1}} \quad .$$

Due to the different topology of M1 and M2 sites, complete disorder (i.e. 50:50 probability of finding Fe or Mg in the M1 and M2 sites) can never be reached at high temperature. This ordering process is therefore described as non-convergent.

During cooling from high temperatures, a displacive process takes place in the pigeonite structure: tetrahedral chains shrink along the *c* axis, becoming two symmetrically distinct chains of tetrahedra, A and B, with S- and O-rotation, respectively (in the sense of Thompson 1970). The space group changes from $C2/c$ to $P2_1/c$. This phase transition is reversible and composition-dependent (Prewitt et al. 1971; Brown et al. 1972; Sueno et al. 1984). The transition temperature decreases with increasing Fe and Ca contents (Prewitt et al. 1971). The thermodynamic character of the transition has been already studied by Smyth (1974), who used a synthetic

pigeonite obtained by inverting an orthopyroxene ($En_{32}Fe_{66}Wo_2$) at high temperature. By in situ annealing of single crystals, Smyth (1974) found a discontinuous character for the phase transition after following the change of intensity of *hkl* reflections with $h + k = 2n + 1$ (*b* reflections) that disappear in space group $C2/c$ as temperature increases. This zone-boundary displacive phase transition is coelastic; it involves a change in space group while the point group symmetry is maintained after the transition. The intensity of *b* reflections is expected to be proportional to the square of the macroscopic ordering parameter (Q_D^2) (Carpenter et al. 1998). Smyth (1974) also observed a significant increase in lattice-volume accompanying the $P2_1/c \rightarrow C2/c$ transition. The structural variations of $P2_1/c$ pyroxene crystals have been followed by in situ annealing in other studies (Prewitt et al. 1971; Brown et al. 1972; Pannhorst 1984; Schröpfer 1985; Shimobayashi and Kitamura 1991; Shimobayashi 1992; Arlt and Armbruster 1997; Arlt et al. 2000; Tribaudino 2000), but in only a few of these were natural crystals used, due to the frequent occurrence of augite exsolution products in natural pigeonites. Arlt and Armbruster (1997) also found a first-order character for the $P2_1/c$–$C2/c$ phase transition in a natural crystal of Ca-poor kanoite. So far, an in situ HT study of the displacive phase transition in an exsolution-free, Ca-rich natural crystal of pigeonite has never been performed. The possible influence of the Ca content on the thermodynamic character of the displacive phase transition is still therefore, unknown. In addition, Arlt et al. (2000) have described a linear relationship between the mean ionic radius at the M2 site and the temperature of the phase transition. It must be anticipated, therefore, that the degree of non-convergent ordering of Fe and Mg between M1 and M2 sites should also affect the temperature of phase transition.

Recently, Pasqual et al. (2000) carried out an ex situ X-ray single-crystal diffraction study of the non-convergent ordering process in an exsolution-free Ca-rich pigeonite crystal with composition close to $En_{50}Fs_{50}$ for which the absence of microstructures has been checked by TEM observations. In this work, Pasqual et al. (2000) calibrated a thermodynamic expression for the cation ordering. The availability of samples free of exsolution products and already calibrated for order/disorder effects by Pasqual et al. (2000) has allowed us to undertake a study of the influence of Ca content on the thermodynamic character of the displacive phase transition when working at equilibrium conditions for the non-convergent process.

Table 1 Crystal data and structure refinements for BTS-308 n.16

CSCC identification code	*hga*	*hgd*	*hgg*	*hgi*	*hgj*
Temperature (°C)	25	650	750	850	950
Space group	$P2_1/c$	$P2_1/c$	$P2_1/c$	$P2_1/c$	$C2/c$
Unit-cell dimensions					
a (Å)	9.719 (7)	9.801 (6)	9.824 (7)	9.840 (5)	9.849 (7)
b (Å)	8.947 (9)	9.008 (8)	9.017 (7)	9.021 (4)	9.018 (6)
c (Å)	5.251 (3)	5.296 (2)	5.309 (3)	5.3184 (11)	5.323 (4)
β (°)	108.49 (5)	109.01 (5)	109.19 (7)	109.35 (3)	109.44 (9)
Volume ($Å^3$)	433.0 (6)	442.1 (5)	444.1 (5)	445.4 (3)	445.8 (5)
Z	4	4	4	4	4
Crystal size (mm^3)	0.297 × 0.231 × 0.231				
Theta range for data collection	2.21–27.52°	2.20–27.52°	2.20–27.51°	2.19–27.49°	2.19–27.50°
Index ranges	−12 < = h < = 11 11 < = k < = 11 0 < = l < = 6	−12 < = h < = 12 11 < = k < = 11 0 < = l < = 6	−12 < = h < = 12 11 < = k < = 11 0 < = l < = 6	−12 < = h < = 12 11 < = k < = 11 0 < = l < = 6	−12 < = h < = 12 11 < = k < = 11 0 < = l < = 6
Reflections collected	2136	2185	2193	2195	1110
Independent reflections	999	1021	1025	1026	519
R (int)	0.019	0.024	0.023	0.022	0.016
Completeness	99.90%	99.90%	100.00%	100.00%	100.00%
Data/restraints/ parameters	999/0/105	1021/0/105	1025/0/105	1026/0/105	519/0/72
Goodness-of-fit on F^2	1.031	0.949	0.894	0.927	1.100
Final R indices [$I > 2\sigma(I)$]	0.0207	0.0256	0.0240	0.0224	0.0271
R indices (all data)	0.0336	0.0550	0.0620	0.0769	0.0627
Extinction coefficient	0.0203 (12)	0.0199 (13)	0.0201 (13)	0.0232 (14)	0.0096 (17)
Largest diff. peak and hole ($e.Å^{-3}$)	0.509 −0.445	0.575 −0.405	0.599 −0.480	0.635 −0.521	0.613 −0.580
Coordinates of 1st peak					
x	0.2461	0.1972	0.2032	0.1960	0.0541
y	0.0929	0.0667	0.0638	0.0649	0.3182
z	0.2707	0.2905	0.2868	0.2873	0.2182

Sampling

Two crystals of a pigeonite sample with composition ca. $En_{47}Fs_{43}Wo_{10}$, extracted from a rhyodacite from Paraná, Brazil (sample BTS-308, previously studied by Pasqual et al. 2000), were selected for this study. They are labelled BTS-308 n.10 and BTS-308 n.16. As reported by Pasqual et al. (2000), TEM observation showed that pigeonite crystals from this sample are exsolution-free. The absence of exsolved augite in this crystal was also carefully checked by analyzing diffraction rocking profiles on a single-crystal X-ray diffractometer.

Experimental methods

In situ annealing experiments

During the X-ray diffraction analysis, the pigeonite crystals were annealed in situ using a microfurnace which has been built at the workshop of the Department of Earth Sciences of Cambridge University specifically for the conventional Philips PW1100 automated four-circle diffractometer. This furnace allows temperatures up to 1100 °C to be reached and intensity data to be collected in the 2θ range of 3–58°.

The crystals were annealed in a sealed quartz vial (1 mm Ø) together with some graphite powder to prevent oxidation of Fe. To avoid any mechanical stress to the crystals, they were kept steady in the vial, using quartz wool.

For crystal BTS-308 n.16, starting from room temperature, and then heating to 650, 750, 800, 825, 850, 875, 900, 925, 950, 975, 1000 °C, lattice parameters were measured by centring 24 selected *hkl a* reflections ($h + k = 2n$). The intensity of *hkl b* reflections ($h + k = 2n + 1$) (102, 052, 702, 233, 233) were measured by step-scan profiles of 3° by ω-rotations. They were scaled with respect to the intensities of adjacent reflections in the same reciprocal row (202, 062, 602, 133, 133). Crystal BTS-308 n.10 was selected as it showed values of the lattice parameters very close to those of crystal n.16 [$a = 9.716$ (3) Å, $b = 8.948$ (3) Å, $c = 5.252$ (3) Å, $\beta = 108.47$ (3), V = 433.1 (3) Å^3], and was annealed, with the same procedure, to check the temperature at which the transition actually occurred. This was done by a careful study of the shape of the rocking curves of *hkl b* reflections with increasing temperature.

Data collection and structure refinement

Complete data collections were performed at 25, 650, 750, 850 and 950 °C on crystal BTS-308 n.16 with the conventional Philips PW1100 automated four-circle diffractometer using graphite-monochromatized Mo $K\alpha$ X-radiation and working at 55 kV and 30 mA. Before each data collection, the crystal was annealed for long enough to reach equilibrium for the Mg/Fe cation ordering following Pasqual et al. (2000). Pairs of equivalent monoclinic reflections ($h\bar{k}l$ and hkl) were collected in the θ range 2–28°. Intensity profiles were integrated following the method of Lehmann and Larsen (1974) modified by Blessing et al. (1974). Intensities were corrected for Lorentz and polarization factors, and for absorption following North et al. (1968). Unit-cell dimensions were calculated from least-squares refinement of the position of ~50 reflections in rows in the range $-28 < \theta < 28°$. Weighted full-matrix least-squared refinements were performed using SHELX-97 (Sheldrick 1997) program. Scattering factors were taken from the International Tables for X-Ray Crystallography (1985). Neutral vs. ionized scattering factors were refined in all the sites that are not involved in chemical substitutions (Hawthorne et al. 1995a). Lattice parameters and information relating to the structure refinements are reported in Table 1. Positional and isotropic displacement parameters are reported in Table 2 and selected interatomic bond distances and angles in Table 3. In Table 3 the distances corrected by ridding motion effects, calculated with program BOND (F. Mazzi, personal communication) using the algorithm of Busing and Levy (1964), are also shown. Anisotropic displacement parameters are reported in Table 4. Site populations, equilibrium distribution coefficients k_D, and order parameters (Q_{QD}) are reported in Table 5 together with the calculated values of Q_D^2 (i.e. I_b/I_a) at each annealing temperature. Observed and calculated structure factors are reported in Table 6, which has been deposited and can be obtained from http://link.springer.de/link/service/journals/00269/index.htm.

Results and discussion

At the end of the structure refinement, a maximum of residual electron density, located at 0.7–0.8 Å from the

Table 2 Atom coordinates ($\times 10^4$) and equivalent Isotropic displacement parameters (Å$^2 \times 10^3$) for crystal BTS-308 n.16 at the different temperature of this work

CSCC code		*hga*	*hgd*	*hgg*	*hgi*	*hgj*
T (°)		25	650	750	850	950
O1A	*x*	8673 (2)	8691 (2)	8696 (3)	8697 (4)	1207 (2)
	y	3383 (2)	3381 (2)	3380 (3)	3378 (4)	889 (2)
	z	1685 (3)	1609 (4)	1587 (5)	1564 (7)	1522 (4)
	U_{eq}	9 (1)	19 (1)	21 (1)	23 (1)	24 (1)
O1B	*x*	3735 (2)	3725 (2)	3724 (3)	3719 (4)	
	y	8367 (2)	8384 (2)	8393 (3)	8400 (4)	
	z	1342 (3)	1418 (4)	1453 (5)	1482 (7)	
	U_{eq}	9 (1)	20 (1)	22 (1)	24 (1)	
O2A	*x*	1215 (2)	1222 (3)	1223 (3)	1237 (5)	3735 (2)
	y	4994 (2)	4968 (2)	4960 (3)	4959 (4)	2446 (2)
	z	3316 (3)	3397 (5)	3426 (6)	3460 (8)	3497 (5)
	U_{eq}	11 (1)	25 (1)	29 (1)	29 (1)	34 (1)
O2B	*x*	6286 (2)	6262 (3)	6256 (3)	6241 (5)	
	y	9881 (2)	9905 (3)	9913 (3)	9921 (5)	
	z	3719 (3)	3632 (5)	3597 (6)	3559 (9)	
	U_{eq}	14 (1)	29 (1)	32 (1)	36 (1)	
O3A	*x*	1042 (2)	1024 (2)	1019 (3)	1019 (4)	3523 (2)
	y	2605 (2)	2516 (3)	2484 (3)	2429 (5)	100 (3)
	z	5758 (4)	5583 (5)	5519 (6)	5446 (9)	382 (4)
	U_{eq}	17 (1)	35 (1)	38 (1)	39 (1)	42 (1)
O3B	*x*	6050 (2)	6031 (2)	6034 (3)	6029 (4)	
	y	7100 (2)	7222 (3)	7273 (3)	7352 (5)	
	z	4806 (3)	5045 (4)	5162 (5)	5284 (9)	
	U_{eq}	13 (1)	31 (1)	36 (1)	41 (1)	
SiA	*x*	426 (1)	435 (1)	439 (1)	445 (2)	2948 (1)
	y	3405 (1)	3398 (1)	3396 (1)	3390 (2)	892 (1)
	z	2761 (1)	2703 (2)	2681 (2)	2659 (3)	2617 (1)
	U_{eq}	7 (1)	15 (1)	17 (1)	18 (1)	19 (1)
SiB	*x*	5493 (1)	5470 (1)	5461 (1)	5451 (2)	
	y	8374 (1)	8381 (1)	8385 (1)	8392 (2)	
	z	2382 (1)	2480 (2)	2525 (2)	2565 (3)	
	U_{eq}	6 (1)	14 (1)	16 (1)	17 (1)	
M1	*x*	2506 (1)	2502 (1)	2502 (1)	2499 (2)	0
	y	6548 (1)	6532 (1)	6530 (1)	6526 (1)	9020 (1)
	z	2317 (1)	2397 (2)	2429 (2)	2463 (4)	1/4
	U_{eq}	6 (1)	18 (1)	20 (1)	22 (1)	24 (1)
M2	x	2552 (1)	2528 (1)	2520 (1)	2514 (2)	0
	y	192 (1)	188 (1)	187 (1)	187 (1)	2688 (1)
	z	2294 (1)	2382 (1)	2414 (2)	2458 (3)	1/4
	U_{eq}	11 (1)	29 (1)	33 (1)	35 (1)	37 (1)

Table 3 Selected interatomic distances (Å) and angles (°) for crystal BTS-308 n.16 at the temperatures of experiments

CSCC code	*hga*		*hgd*		*hgg*		*hgi*		*hgj*	
T (°C)	25	r.m.[a]	650	r.m	750	r.m.	850	r.m.	950	r.m.
SiA–O1A	1.616 (2)	1.617	1.617 (3)	1.621	1.618 (3)	1.622	1.623 (4)	1.628	1.618 (2)	1.623
SiA–O2A	1.598 (2)	1.601	1.595 (3)	1.606	1.593 (3)	1.605	1.604 (4)	1.615	1.594 (2)	1.610
SiA–O3A	1.658 (2)	1.667	1.649 (2)	1.666	1.645 (3)	1.665	1.647 (4)	1.668	1.653 (2)	1.675
SiA–O3A	1.637 (2)	1.645	1.641 (2)	1.657	1.643 (3)	1.662	1.641 (4)	1.658	1.641 (2)	1.662
< SiA–O >	1.627	1.633	1.625	1.638	1.625	1.639	1.629	1.642	1.627	1.642
TILT	4.12 (6)		4.73 (5)		4.89 (7)		5.18 (4)		5.08 (9)	
Vol	2.189		2.185		2.183		2.200		2.191	
TQE	1.0070		1.0061		1.0058		1.0052		1.0053	
TAV	28.70		24.85		23.66		21.32		21.54	
SiB–O1B	1.621 (2)	1.623	1.616 (3)	1.621	1.612 (3)	1.616	1.608 (4)	1.614		
SiB–O2B	1.600 (2)	1.608	1.598 (3)	1.610	1.594 (3)	1.609	1.586 (5)	1.603		
SiB–O3B	1.666 (2)	1.671	1.651 (2)	1.674	1.663 (3)	1.681	1.658 (4)	1.679		
SiB–O3B	1.663 (2)	1.678	1.659 (2)	1.665	1.645 (3)	1.663	1.644 (4)	1.666		
< SiB–O >	1.637	1.645	1.631	1.643	1.628	1.642	1.624	1.640		
TILT	5.56 (6)		5.50 (5)		5.31 (7)		5.08 (4)			
Vol	2.238		2.211		2.201		2.180			
TQE	1.0047		1.0048		1.0050		1.0058			
TAV	19.22		19.52		20.42		23.18			
M1–O1A	2.051 (2)	2.052	2.064 (3)	2.064	2.071 (3)	2.071	2.075 (4)	2.076	2.072 (2)	2.081
M1–O1A	2.159 (2)	2.160	2.195 (3)	2.195	2.201 (3)	2.202	2.201 (4)	2.203	2.222 (2)	2.222
M1–O1B	2.175 (2)	2.176	2.212 (3)	2.213	2.223 (3)	2.224	2.233 (4)	2.234	2.222 (2)	2.222
M1–O1B	2.073 (2)	2.074	2.077 (3)	2.077	2.079 (4)	2.080	2.077 (4)	2.078	2.072 (2)	2.081
M1–O2A	2.049 (2)	2.052	2.067 (3)	2.074	2.073 (3)	2.081	2.064 (4)	2.071	2.076 (3)	2.076
M1–O2B	2.075 (2)	2.081	2.084 (3)	2.092	2.084 (3)	2.093	2.092 (5)	2.103	2.076 (3)	2.076
< M1–O >	2.097	2.099	2.117	2.119	2.122	2.125	2.124	2.127	2.123	2.126
Vol	12.172		12.508		12.604		12.632		12.616	
OQE	1.0073		1.0080		1.0081		1.0085		1.0086	
M2–O1A	2.174 (2)	2.175	2.186 (3)	2.189	2.187 (3)	2.190	2.183 (4)	2.184	2.174 (2)	2.178
M2–O1B	2.145 (2)	2.146	2.161 (3)	2.164	2.161 (3)	2.165	2.163 (4)	2.169	2.174 (2)	2.178
M2–O2A	2.087 (2)	2.089	2.086 (3)	2.092	2.085 (4)	2.091	2.085 (5)	2.092	2.083 (3)	2.089
M2–O2B	2.040 (2)	2.041	2.059 (3)	2.062	2.065 (4)	2.069	2.068 (5)	2.072	2.083 (3)	2.089
M2–O3A	3.438 (3)	3.439	3.328 (3)	3.329	3.284 (3)	3.285	3.214 (5)	3.217	3.152 (3)	3.153
M2–O3A	2.437 (2)	2.438	2.538 (3)	2.539	2.574 (4)	2.576	2.625 (5)	2.628	2.651 (3)	2.653
M2–O3B	2.954 (3)	2.954	2.835 (3)	2.837	2.778 (4)	2.779	2.700 (5)	2.700	2.651 (3)	2.653
M2–O3B	2.633 (2)	2.633	2.861 (3)	2.861	2.949 (3)	2.950	3.063 (5)	3.064	3.152 (3)	3.153
< M2–O > x6	2.253	2.254	2.315	2.318	2.337	2.340	2.364	2.368	2.386	2.390
< M2–O > x7	2.745	2.746	2.788	2.791	2.800	2.803	2.814	2.818	2.828	2.832
O3A–O3A	2.632 (2)	2.633	2.648 (1)	2.649	2.655 (2)	2.655	2.662 (1)	2.663	2.668 (2)	2.670
O3B–O3B	2.721 (2)	2.722	2.695 (1)	2.698	2.686 (2)	2.688	2.673 (1)	2.675		
O3A–O3A–O3A	188.21 (14)		181.3 (2)		178.8 (3)		174.5 (4)		172.24 (16)	
O3B–O3B–O3B	149.52 (13)		158.6 (2)		162.4 (3)		168.5 (4)			
O3A–M2–O3A	49.73 (13)		51.55 (7)		52.20 (8)		53.09 (11)		53.90 (7)	
O3B–M2–O3B	57.96 (7)		56.47 (7)		55.84 (8)		54.83 (11)			

[a] r.m. = ridding motion-corrected distances

M2 site, was observed in the difference Fourier map. The coordinates of this maximum are reported in Table 1; attempts to refine them were unsuccessful. It is well known that a split position of the M2 site, along the diad axis, labelled M2, is found in diopside (Rossi et al. 1987; Tribaudino et al. 1989). The *y* coordinate of the M2 site in diopside (occupied by Fe), recalculated in the unit cell of pigeonite, corresponds to the *y* coordinate of the M2 site of pigeonite (occupied by Fe and Mg), while the *y* coordinate of the M2 site of diopside (occupied by Ca) corresponds to that of the residual peak found in pigeonite. This split position in pigeonite is still present after the phase transition (Table 1) and is therefore likely to be occupied by Ca. In order to check the real nature of this split, high-resolution data are necessary, and work is in progress using an excellent-quality crystal from the same sample (F. Cámara et al., personal communication).

The site populations of M1 and M2 sites at each *T* (Table 5) were calculated with a modified version (Zema et al. 1997) of the routine MINUIT (James and Roos 1975) using the structure refinement data obtained for each *T* and microprobe data from Pasqual et al. (2000). The degree of Fe^{2+}–Mg non-convergent ordering was measured at each *T* by means of the intracrystalline distribution coefficient k_D, expressed as

$$k_D = \frac{X_{Fe}^{M1}\left(1 - X_{Fe}^{M2}\right)}{X_{Fe}^{M2}\left(1 - X_{Fe}^{M1}\right)} \quad , \qquad (1)$$

where X_{Fe}^{M1} is the atomic fraction of Fe* (Fe* = Fe^{2+} + Mn), i.e. Fe*/(Fe* + Mg) at the M1 site, and X_{Fe}^{M2} is the

Table 4 Anisotropic displacement parameters[a] ($Å^2 \times 10^3$) for BTS-308 n.16

T (°C)		25	650	750	850	950
O1A	U^{11}	0.753	14 (1)	12 (1)	16 (2)	18 (1)
	U^{22}	9 (1)	24 (1)	27 (2)	29 (2)	30 (1)
	U^{33}	10 (1)	19 (1)	21 (1)	23 (2)	24 (1)
	U^{23}	0 (1)	1 (1)	−2 (1)	−5 (2)	−1 (1)
	U^{13}	2 (1)	5 (1)	3 (1)	5 (2)	5 (1)
	U^{12}	0 (1)	1 (1)	1 (1)	1 (2)	1 (1)
O1B	U^{11}	7 (1)	14 (1)	19 (1)	17 (2)	
	U^{22}	9 (1)	23 (1)	24 (2)	29 (2)	
	U^{33}	11 (1)	21 (1)	23 (1)	24 (2)	
	U^{23}	1 (1)	−1 (1)	1 (1)	4 (2)	
	U^{13}	3 (1)	4 (1)	6 (1)	5 (2)	
	U^{12}	0 (1)	1 (1)	1 (1)	1 (2)	
O2A	U^{11}	12 (1)	30 (1)	36 (2)	35 (3)	39 (1)
	U^{22}	7 (1)	17 (1)	19 (2)	16 (2)	26 (1)
	U^{33}	14 (1)	32 (1)	35 (1)	36 (2)	40 (1)
	U^{23}	−1 (1)	−3 (1)	−3 (1)	−5 (2)	−9 (1)
	U^{13}	6 (1)	14 (1)	16 (1)	12 (2)	17 (1)
	U^{12}	−2 (1)	−8 (1)	−8 (1)	−10 (2)	−13 (1)
O2B	U^{11}	14 (1)	30 (1)	31 (2)	38 (3)	
	U^{22}	11 (1)	26 (2)	30 (2)	36 (3)	
	U^{33}	21 (1)	32 (1)	36 (2)	39 (2)	
	U^{23}	−8 (1)	−10 (1)	−12 (1)	−11 (2)	
	U^{13}	11 (1)	14 (1)	14 (1)	20 (2)	
	U^{12}	−6 (1)	−11 (1)	−12 (1)	−15 (2)	
O3A	U^{11}	7 (1)	18 (1)	21 (2)	20 (2)	27 (1)
	U^{22}	22 (1)	52 (2)	58 (2)	61 (3)	61 (2)
	U^{33}	21 (1)	32 (1)	34 (2)	35 (2)	37 (1)
	U^{23}	13 (1)	23 (1)	26 (1)	28 (2)	−27 (1)
	U^{13}	4 (1)	6 (1)	8 (1)	6 (2)	10 (1)
	U^{12}	2 (1)	3 (1)	6 (1)	5 (2)	−4 (1)
O3B	U^{11}	8 (1)	21 (1)	22 (2)	27 (2)	
	U^{22}	17 (1)	43 (1)	51 (2)	58 (3)	
	U^{33}	14 (1)	29 (1)	36 (2)	40 (2)	
	U^{23}	6 (1)	19 (1)	22 (1)	24 (2)	
	U^{13}	3 (1)	9 (1)	10 (1)	12 (2)	
	U^{12}	0 (1)	4 (1)	3 (1)	2 (2)	
SiA	U^{11}	6 (1)	14 (1)	16 (1)	17 (1)	17 (1)
	U^{22}	6 (1)	16 (1)	18 (1)	19 (1)	19 (1)
	U^{33}	10 (1)	16 (1)	17 (1)	19 (1)	19 (1)
	U^{23}	−1 (1)	−2 (1)	−2 (1)	−4 (1)	−2 (1)
	U^{13}	4 (1)	6 (1)	6 (1)	7 (1)	6 (1)
	U^{12}	−1 (1)	−1 (1)	−2 (1)	−3 (1)	−2 (1)
SiB	U^{11}	6 (1)	13 (1)	14 (1)	14 (1)	
	U^{22}	5 (1)	15 (1)	16 (1)	19 (1)	
	U^{33}	8 (1)	16 (1)	18 (1)	18 (1)	
	U^{23}	−1 (1)	−1 (1)	−1 (1)	1 (1)	
	U^{13}	3 (1)	5 (1)	5 (1)	5 (1)	
	U^{12}	−1 (1)	−2 (1)	−2 (1)	−2 (1)	
M1	U^{11}	7 (1)	19 (1)	21 (1)	23 (1)	26 (1)
	U^{22}	6 (1)	19 (1)	22 (1)	24 (1)	25 (1)
	U^{33}	7 (1)	16 (1)	18 (1)	19 (1)	20 (1)
	U^{23}	0 (1)	0 (1)	0 (1)	−3 (1)	
	U^{13}	3 (1)	5 (1)	5 (1)	5 (1)	6 (1)
	U^{12}	0 (1)	0 (1)	0 (1)	0 (1)	
M2	U^{11}	9 (1)	29 (1)	33 (1)	36 (1)	38 (1)
	U^{22}	16 (1)	34 (1)	38 (1)	41 (1)	43 (1)
	U^{33}	8 (1)	20 (1)	22 (1)	24 (1)	25 (1)
	U^{23}	3 (1)	2 (1)	1 (1)	−2 (1)	
	U^{13}	1 (1)	2 (1)	2 (1)	3 (1)	3 (1)
	U^{12}	1 (1)	3 (1)	5 (1)	7 (1)	

[a] The anisotropic displacement factor exponent takes the form: $-2\pi^2[h^2a^{*2}U^{11} + \cdots + 2hka^*b^*U^{12}]$

Table 5 Site occupancies calculated with MINUIT procedure for BTS-308 n.16 at each T of experiment

T (°C)	25	650	750	850	950
Mg^{M1}	0.7668	0.7529	0.7267	0.7108	0.6900
Fe^{M1}	0.2082	0.2222	0.2474	0.2625	0.2820
Mn^{M1}	0.0067	0.0072	0.0080	0.0085	0.0091
Mg^{M2}	0.1596	0.1699	0.2008	0.2137	0.2457
Fe^{M2}	0.6245	0.6148	0.5845	0.5722	0.5401
Mn^{M2}	0.0206	0.0202	0.0194	0.0189	0.0182
Q_{OD}	0.5002	0.4692	0.4056	0.3713	0.3146
Q_D^2	0.3026	0.0963	0.0489	0.0140	0.0048
X_{Fe}^{M1}	0.2189	0.2335	0.2601	0.2760	0.2967
X_{Fe}^{M2}	0.8017	0.7889	0.7505	0.7345	0.6944
K_D	0.0693	0.0815	0.1169	0.1378	0.1857
$Ln(K_D)$	−2.6688	−2.5069	−2.1468	−1.9817	−1.6838
1/T (K)	0.00114	0.00108	0.00098	0.00089	0.00082
1/T ($°C^{-1}$)	0.00166	0.00154	0.00133	0.00118	0.00105
T (°C)[a]	604	650	774	843	992

[a] T calculated with Pasqual et al. (2000) equation for BTS-308 n.2

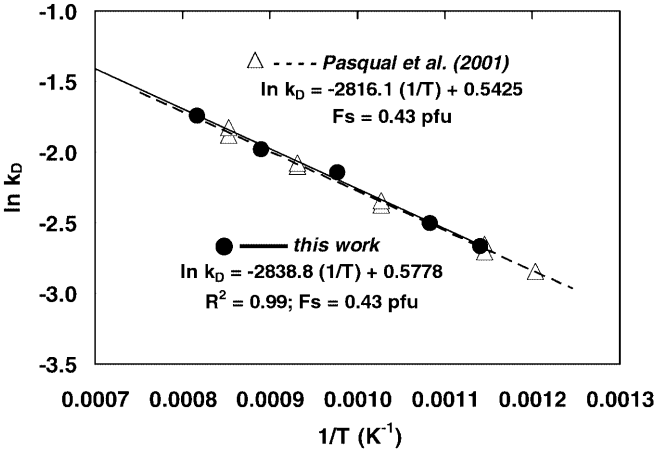

Fig. 1 Variation of ln k_D with $1/T$ (K^{-1}). *Filled dots* represent data of crystal BTS-308 n.16 of this study. *Open triangles* represent data of crystal BTS-308 n.2 studied by Pasqual et al. (2000). *Dashed line* represents the solution to the thermometric expression obtained by Pasqual et al. (2000) using data obtained in ex situ annealing experiments

same for M2 site. The k_D values are reported in Table 5. At each temperature they are in perfect agreement with the equation $\ln k_D = -2816(\pm 83)/T(\mathrm{K}) + 0.542(\pm 0.083)$ derived by Pasqual et al. (2000) by statistical regression of $\ln k_D$ as a function of X_{Fe} and T. In Fig. 1 we report the $\ln k_D$ and $1/T$ data of Pasqual et al. (2000) for a crystal of the same sample and those of this study. They all plot over the same $\ln k_D$-$(1/T)$ line confirming that equilibrium cation order was achieved before each data collection. The very good agreement between the two sets of data testifies to the good calibration of both ex situ and in situ annealing systems and to the fact that the Fe–Mg exchange reaction in this pigeonite sample, at these temperatures, is quenchable.

As can be seen in Fig. 2a, the evolution of the ratio I_b/I_a in crystals n.10 and n.16 shows a continuous

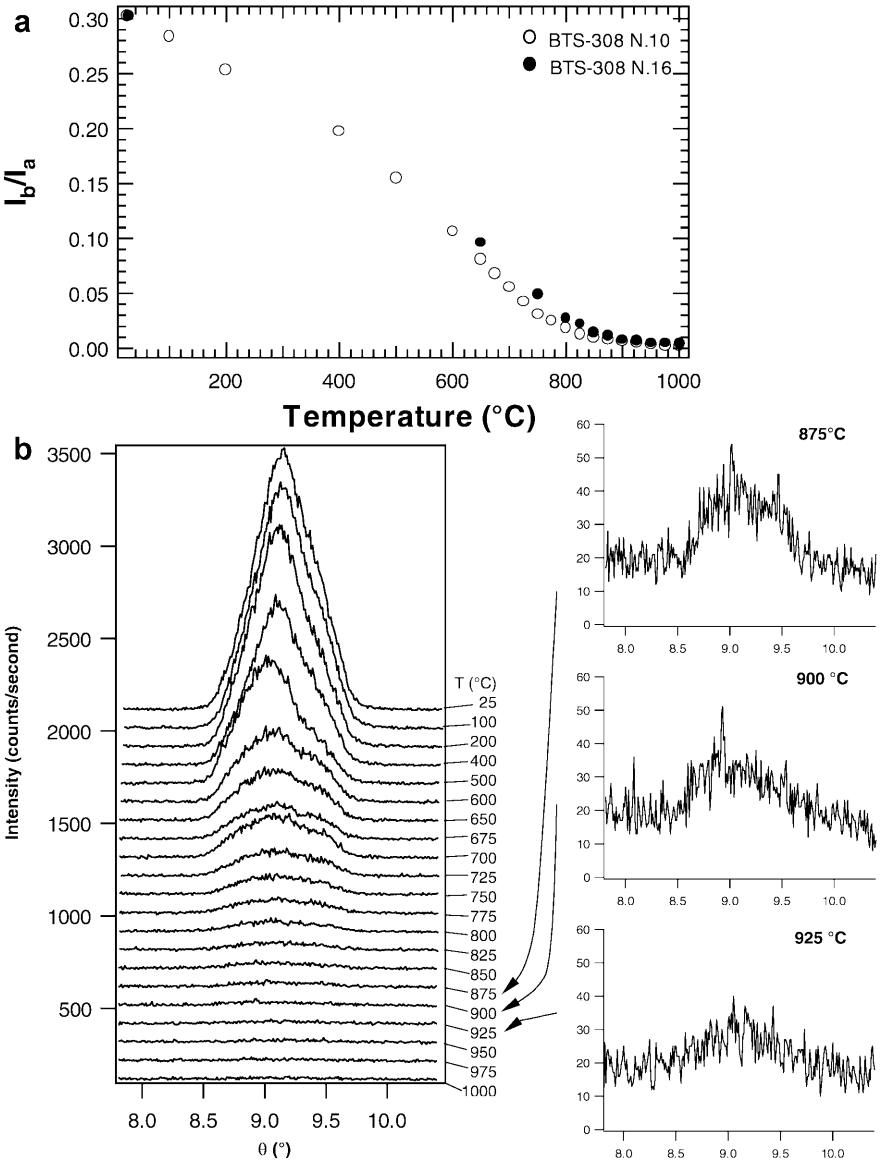

Fig. 2 **a** Variation of the intensity ratio I_b/I_a versus temperature. I_b represents the intensity of selected *hkl* reflections with $h + k = 2n + 1$ and I_a the intensity of *hkl* reflections with $h + k = 2n$. A continuous decrease of the intensity ratio occurs up to high temperature. **b** Variation of the profile shape of the reflection (102) as the temperature increase. *On the right side* the vertical scale has been expanded for three temperatures around T_c. A sharp diffraction profile is still evident at 875 °C. At higher temperatures the integrated intensity appears to correspond only to diffuse scattering

transition from the room-temperature $P2_1/c$ to the high-temperature $C2/c$ phase, thus confirming the observations on Mull pigeonite by Brown et al. (1972), who recorded a slowly disappearance of class *b* reflections. A similar behaviour has been observed by Tribaudino (2000) in synthetic samples with composition within the range Di40En60 and Di60En40. The careful analysis of the rocking curves with increasing temperature for reflection (102) in crystal n.10 (see Fig. 2b) shows that a sharp diffraction profile is still present at 875 °C. At 925 °C, the diffracted intensity appears to be diffuse scattering; the transition is likely to have occurred at some temperature between 875 and 925 °C. For this reason, the structure refinement of data collected on crystal n.16 at 950 °C was carried out in space group $C2/c$. In Fig. 3 the variation of the lattice parameters of crystal n.16 with increasing temperature was compared with that of the low-Ca pigeonite studied by Smith (1974). The variation of monoclinic angle is better shown as $c\sin\beta$ (Boffa-Ballaran et al. 2000). In particular, neither a significant volume increase nor an abrupt change in the cell parameters, as shown by the low-Ca pigeonite, were recorded. The continuous character of the transition was also evidenced by the behaviour, with increasing T, of some geometrical parameters related to the distortion of the structure. One feature of this $P2_1/c$–$C2/c$ displacive phase transition is the extension of the two different chains by rotation of the tetrahedra. This can be followed by the variation of *kinking* angle, i.e. the O3–O3–O3 angle of A and B chains (Table 3). In Fig. 4 the variation with temperature of the *kinking* angle of both chains from this study is compared with the variation of the same parameter in the Ca-free crystal studied by Smyth (1974) and in the kanoite studied by Arlt and Armbruster (1997). The data of Pasqual et al. (2000), obtained at room temperature after annealing at high temperatures with subsequent quenching, were also shown. It is evident from this plot that, while the data by

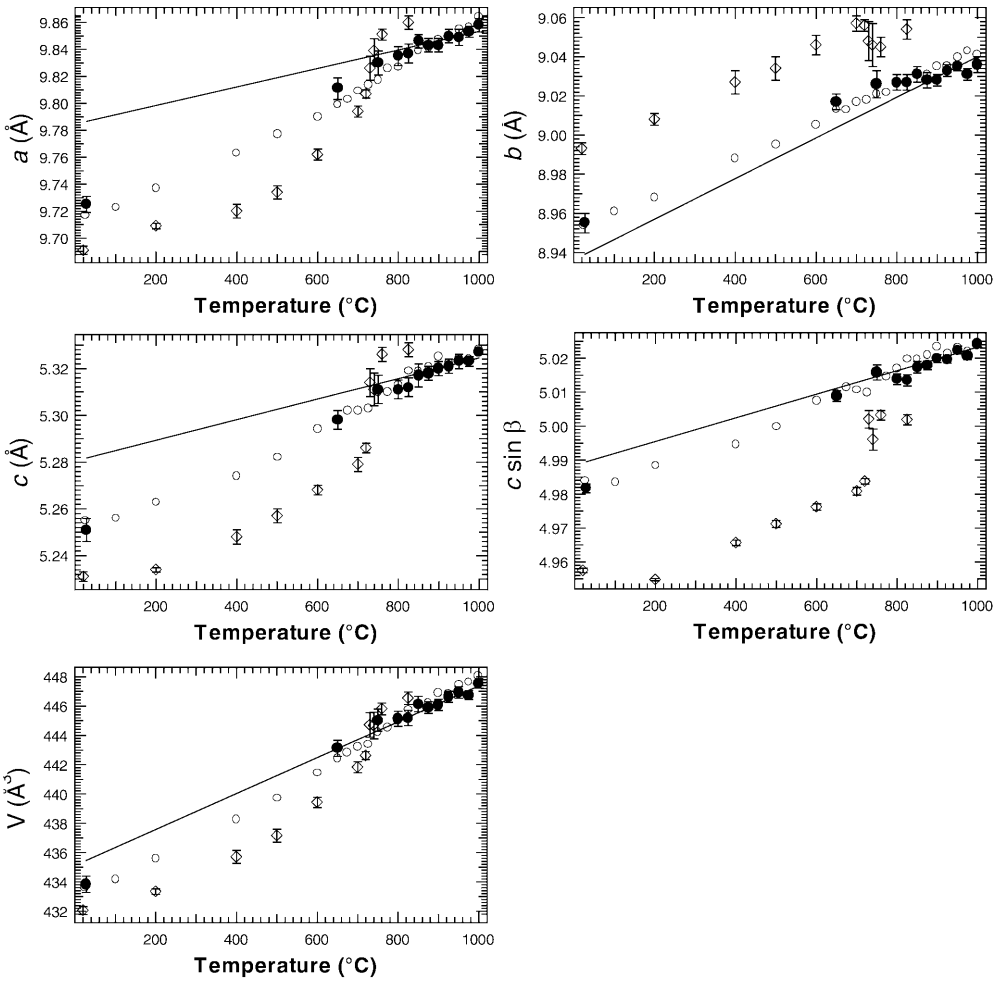

Fig. 3 Variation of lattice parameters with increasing temperature for crystals BTS-308 n.10 (*open circles*) and BTS-308 n.16 (*filled circles*). Lattice parameter data for the low-Ca clinopyroxene studied by Smyth (1974) has also been plotted (*open diamonds*) for comparison. *Error bars* represent 1σ. *Straight lines* are extrapolation from the highest temperature data points to show the expected variation of cell parameters for the $C2/c$ structure of crystal BTS-308

Pasqual et al. (2000) show a negligible variation in the *kinking* angle, all the in situ high-temperature data show a significant variation. It is also evident from Fig. 4 that, while pigeonite with little Ca content and kanoite show a sudden extension of the B chain and a strong change in rotation in A chain (which passes from S rotation to O rotation) at the transition temperature, the Ca-rich crystal of this study shows a continuous extension of the B chain and a progressive change in rotation of the A chain.

Another interesting parameter related to the tetrahedral chains is the value of the out-of-plane tilting angle, TILT (Cameron et al. 1973), which is different for each chain at room temperature and converges at the transition temperature (Table 3). Tetrahedra of the B chain are more tilted than tetrahedra of the A chain at room temperature. However, this parameter is likely to be also related to the degree of non-convergent cation ordering, as was observed for the B chain in orthopyroxene (Tarantino et al. 2001), and it is difficult to distinguish the contribution of the displacive transition alone.

The distortion of an Si–O tetrahedron from its ideal configuration can be described by the tetrahedral angle variance (TAV), as defined by Robinson et al. (1971). A-chain tetrahedra are more distorted than B-chain tetrahedra at room temperature, and the relevant TAV values of both converge at the transition temperature, with A-chain tetrahedra becoming more regular and B-chain tetrahedra more distorted.

The rotation of tetrahedra by extension and rotation of the chains involves a change in coordination at the M2 site. This effect can be followed by examining the variation of the short and long M2–O3B bond distances. The short M2–O3B distance increases up to 3.152 Å, giving an effective reduction of the coordination number of M2 site from 6 + 1 to 6. In contrast, the long M2–O3B distance shrinks at the phase transition and approaches the M2–O3A short distance. In Fig. 5, variations of M2–O3B distances are shown for the crystal used in this study and for the magnesian–clinoferrosilite crystal studied by Smyth (1974). Again, the change in coordination of M2 site occurs in a sudden way for the Ca-poor crystal studied by Smyth (1974), while the Ca-rich crystal of this study displays a progressive change of bond distances with increasing temperature.

From Fig. 4 it is evident that the Ca-rich pigeonite of this study exhibits less spontaneous strain after the $C2/c$–$P2_1/c$ phase transition than the Ca-poor crystal stud-

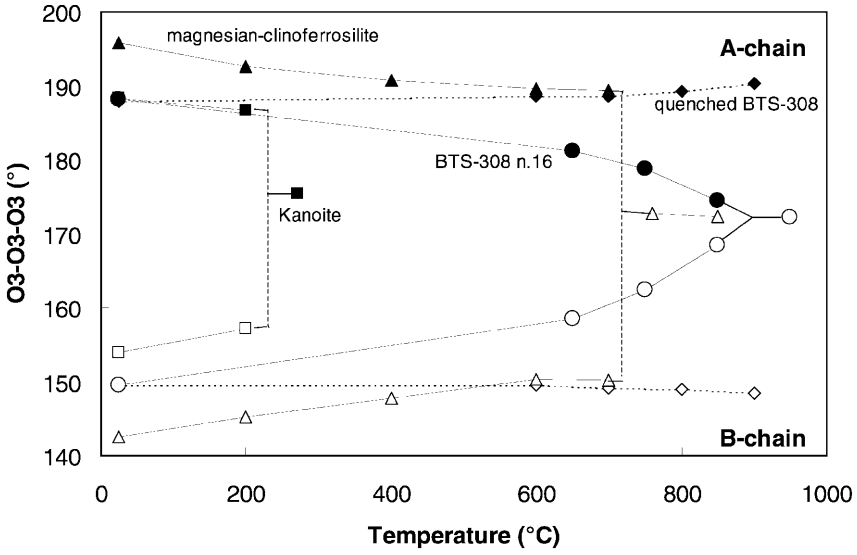

Fig. 4 Variation of *kinking* O3–O3–O3 angle of *A and B chains* with increasing temperature. *Filled circles* represent values for the A chain and *empty symbols* values for the B chain; *dots* BTS-308 n.16; *triangles* magnesian–clinoferrosilite (Smyth 1974); *squares* kanoite (Arlt and Armbruster 1997); *diamonds* BTS-308 n.2 by Pasqual et al. (2000). Ex situ data show a slight shrinking of tetrahedral chains while in situ data show extension and rotation of tetrahedra chains. *BTS-308 n.16* shows continuous variation of *kinking* angles, while kanoite and magnesian-clinoferrosilite show a discontinuous change of the same parameter at the transition point

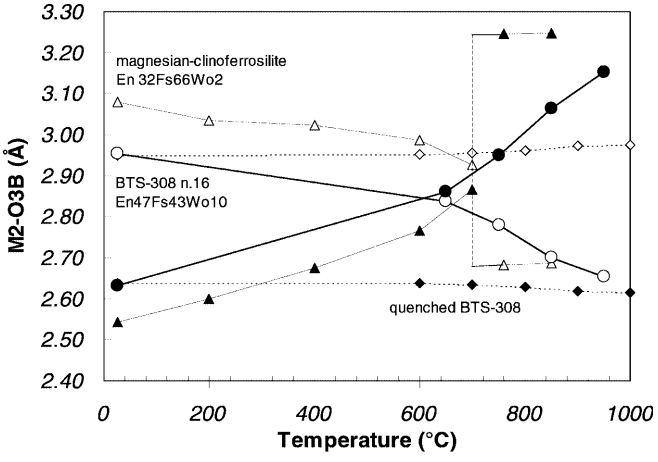

Fig. 5 Variation of M2–O3B interatomic bond distance with increasing temperature. Symbols as in Fig. 4. *Filled symbols* represent the short M2–O3B distance at room temperature and *open symbols* the long M2–O3B distance. While no clear change can be seen in the room-temperature data, Ca-poor magnesian-clinoferrosilite crystal exhibits a sudden change in coordination at the transition temperature. In contrast, crystal BTS-308 n.16 exhibits a continuous extension of the short M2–O3B bond distance and a continuous shrinkage of the long M2–O3B bond distance

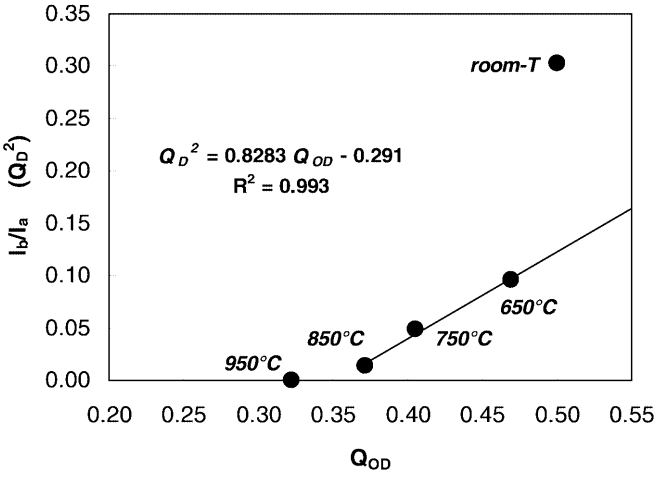

Fig. 6 Plot of the square of the macroscopic displacive order parameter (Q_D^2) expressed as the intensity ratio I_b/I_a vs. the macroscopic non-convergent order parameter (Q_{OD}) for the crystal of this study. Except for the room-temperature datum, the data define equilibrium variations, and a *straight line* has been fitted to them

ied by Smyth (1974). Although the latter is slightly richer in Fe, it is evident that Ca content and the macroscopic strain are linked — the strain is reduced by increasing the Ca content. At the same time, the Ca content seems to be related to the change in thermodynamic character of the transition from first to second order, and this is consistent with a change in the fourth-order coefficient of Landau expansion for the transition due to strain/order parameter coupling. The behaviour exhibited by M2–O3 bond distances with increasing T and the observed presence of a split M2 site could suggest a microscopic model at the atomic scale to explain the change in character of the phase transition related to the Ca content of the sample. Since the second position of the split M2 site could correspond to the actual Ca position, the larger ionic radius of Ca and its shifting towards the tetrahedral chains allow it to coordinate with one O3 A and two O3B oxygen atoms at room temperature, giving rise to a coordination 6 + 1. At high temperatures, the expansion of the unit cell would enlarge the interatomic bond distances in the coordination environment of the M2 site and would lead to the weakening of the M2–O3B bonds. In particular, if the atomic species present at M2 is a cation with small ca-

tion radius (e.g. Mg), at a certain temperature the long M2–O3B bonds would break and the chains would gain freedom to rotate. Chain extension could thus happen abruptly and the phase transition would be discontinuous. However, if Ca atoms are present at a shifted M2 position, both O3B atoms would still be bonded to the Ca atom and maintain the strength of M2–O3B bonds. Ca atoms would act as point defects at very diluted concentrations, and the strength fields due to the presence of a Ca atom at M2 would not become important until the Ca concentration reached a critical value. At that point the breaking of M2–O3B bonds (when M2 is occupied by Mg or Fe) would be counterbalanced by M2–O3 distances still supported by the presence of Ca, and the tetrahedra would not be able to rotate freely. The phase transition would then be expected to become continuous, as we observed in our study sample.

It is evident that all the variations in geometrical parameters described above for the Ca-rich pigeonite of this study are compatible with a continuous phase transition against the first-order character found by Smyth (1974) and Arlt and Armbruster (1997) for Ca-poor crystals. It is possible that the thermodynamic character of the displacive phase transition depends on the Ca content. Moreover, an increase in Ca content at the M2 site, enlarging the effective mean radius at the M2 site, should also reduce the transition temperature, following the hypothesis by Prewitt et al. (1971) and Arlt et al. (2000). Note, however, that Pasqual et al. (2000) described a faint mottled texture on a TEM scale in pigeonite crystals from the same rock as used here. They suggested that this might be due to the earliest stage of exsolution. The associated strain effects could also influence the thermodynamic character of the displacive phase transition (see also Tribaudino et al. 2001). In our sample, we still observe a $P2_1/c$ structure at 850 °C, well above the transition temperature found by Smyth (1974) for a Ca-poor crystal. Although Smyth's (1974) Ca-poor crystal had higher Fs content, which also lowers the transition temperature (Prewitt et al. 1971), the higher T_c found for our sample could be due to the fact that the equilibrium degree of Mg–Fe non-convergent ordering at high temperature reduces the effective mean radius at the M2 site (on disordering, Fe leaves the M2 site and enters the M1 site) and counteracts the enlargement due to Ca. For a fixed Ca content, the lower the degree of non-convergent ordering, the higher should be the critical temperature of the displacive phase transition. This would account for the fact that the variation of I_b/I_a appears to show a long tail at high T rather than showing a linear decrease to a discrete transition point, T_c, more typical of a classical second-order transition. Q_D and Q_{OD} are thus coupled-order parameters. In the simplest case, coupling of the form $\lambda Q_D^2 Q_{OD}$ is expected, and this might lead to a linear relationship between Q_D^2 and Q_{OD}. In Fig. 6 the intensity ratio I_b/I_a, considered to be proportional to Q_D^2 is plotted vs. Q_{OD}. Excluding the room-temperature data point, which is not in equilibrium with respect to Q_{OD}, we observe an approximately linear relation that can be expressed by the linear regression $Q_D^2 = 0.8283\ Q_{OD} - 0.291$; $R^2 = 0.99$.

Acknowledgements Financial support from the European TMR network Mineral Transformations, contract no. ERB-FMRX-CT97–0108 and the Italian MURST project Transformation, Reactions, Ordering in Minerals are gratefully acknowledged. We thank D. Pasqual (University of Padova, Italy), who provided us with the sample BTS-308, and Mario Tribaudino for thoughtful comments on the manuscript.

References

Arlt T, Armbruster T (1997) The temperature-dependent $P2_1/c$–$C2/c$ phase transition in the clinopyroxene kanoite $MnMg[Si_2O_6]$: a single-crystal X-ray and optical study. Eur J Mineral 9: 953–954

Arlt T, Kunz M, Stolz J, Ambruster T, Angel RJ (2000) P–T–X data on $P2_1/c$ clinopyroxenes and their displacive phase transitions. Contrib Mineral Petrol 138: 35–45

Blessing RH, Coppens P, Becker P (1974) Computer analysis of step scanned X-ray data. J Appl Crystallogr 7: 488–492

Boffa Ballaran T, Angel RJ, Carpenter MA (2000) High-pressure transformation behaviour of the cummingtonite-grunerite solid solution. Eur J Mineral 12: 1195–1213

Brown GE, Prewitt CT, Papike JJ, Sueno S (1972) A comparison of the structures of low and high pigeonite. J Geophys Res 77: 5778–5789

Busing WR, Levy HA (1964) The effect of thermal motion on the estimation of bond lengths from diffraction measurements. Acta Crystallog 17: 142–146

Cameron M, Sueno S, Prewitt CT, Papike JJ (1973) High-temperature crystal chemistry of acmite, diopside, hedenbergite, jadeite, spodumene and ureyite. Am Mineral 59: 594–618

Carpenter MA, Salje EKH, Graeme-Barber A (1998) Spontaneous strain as a determinant of thermodynamic properties for phase transition in minerals. Eur J Mineral 10: 621–691

Hawthorne FC, Ungaretti L, Oberti R (1995) Site populations in minerals: terminology and presentation of results of crystal-structure refinement. Can Mineral 33: 907–911

International tables, vol A. Hahn T (ed) International tables for crystallography, vol A. Kluwer Academic Publishers, Dordrecht, The Netherlands, 1995

International tables, vol C. Wilson AJC (ed) International tables for crystallography, vol C. Kluwer Academic Publishers, Dordrecht, The Netherlands, 1995

James F, Roos M (1975) MINUIT, a system fur function minimization and analysis of the parameter error and correlations. Comput Phys Commun 10: 343–347, CERN/DD, Int Rep 75/20

Lehmann MS, Larsen FK (1974) A method for location of the peaks in step-scan-measured Bragg reflections. Acta Crystallogr (A)30: 580–584

North ACT, Phillips DC, Mathews FS (1968) A semi-empirical method of absorption correction. Acta Crystallogr (A)24: 351–359

Pannhorst W (1984) High-temperature crystal structure refinements of low clinoenstatite up to 700 °C. Neues Jb Miner Abh 150: 219–228

Pasqual D, Molin G, Tribaudino M (2000) Single-crystal thermometric calibration of Fe–Mg order–disorder in pigeonites. Am Mineral 85: 953–962

Prewitt CT, Brown GE, Papike JJ (1971) Apollo 12 clinopyroxenes. High-temperature X-ray diffraction studies. Geochim Cosmochim Acta Suppl 2, 1: 59–68

Robinson K, Gibbs GV, Ribbe PH (1971) Quadratic elongation: a quantitative measure of distortion in coordination polyhedra. Science 172: 567–570

Rossi G, Oberti, R, Dal Negro A, Molin GM, Mellini M (1987) Residual electron density at the M2 site in $C2/c$ clinopyroxenes:

relationships with bulk chemistry and sub-solidus evolution. Phys Chem Miner 14: 514–520
Schröpfer L (1985) Observation of reactions in synthetic Ca-poor pyroxene single crystals at elevated temperatures by X-ray diffraction. Phys Chem Miner 12: 49–54
Sheldrick GM (1997) Programs for crystal structure analysis (release 97–2). Institut für anorganische Chemie der Universität, Tammanstrasse 4, 3400 Göttingen, Germany, 1998
Shimobayashi N (1992) Direct observation of antiphase domain boundaries in pigeonite. Am Mineral 77: 107–114
Shimobayashi N, Kitamura M (1991) Phase transition in Ca-poor clinopyroxenes. A high-temperature transmission electron microscopic study. Phys Chem Miner 18: 153–160
Smyth JR (1974) The high-temperature crystal chemistry of clinohypersthene. Am Mineral 59: 1069–1082
Sueno S, Kimata M, Prewitt CT (1984) The crystal structure of high clinoferrosilite. Am Mineral 69: 264–269
Tarantino SC, Domeneghetti MC, Carpenter MA, Shaw CJS, Tazzoli V (2002) Mixing properties of enstatite-ferrosilite solid solution: I A macroscopic perspective. Eur J Mineral 14: 525–536
Thompson JB Jr (1970) Geometrical possibilities for amphiboles structures: model biopyriboles. Am Mineral 55: 292–293
Tribaudino M (2000) A transmission electron microscope investigation of the $C2/c \rightarrow P2_1/c$ phase transition in clinopyroxenes along the diopside-enstatite ($CaMgSi_2O_6$-$Mg_2Si_2O_6$) join. Am Mineral 85: 707–715
Tribaudino M, Benna P, Bruno E (1989) Average structure and M2 site configurations in $C2/c$ clinopyroxenes along the Di–En join. Contrib Mineral Petrol 103: 452–456
Tribaudino M, Nestola F, Cámara F, Domeneghetti MC (2002) The high-temperature $C2/c \rightarrow P2_1/c$ phase transition in Fe-free pyroxene ($Ca_{0.15}Mg_{1.85}Si_2O_6$): structural and thermodynamic behaviour. Am Mineral 87: 648–657
Williams J, Takeda H (1972) Trans Am Geophys Union 53: 551
Zema M, Domeneghetti MC, Molin GM, Tazzoli V (1997) Cooling rates of diogenites: a study of Fe^{2+}–Mg ordering in orthopyroxene by X-ray single-crystal diffraction. Meteor Planet Sci 32: 855–862